1 km-resolution maps reveal increases in above- and belowground forest biomass carbon pools in China over the past 20 years

Yongzhe Chen[1,2], Xiaoming Feng[1,2,*], Bojie Fu[1,2], Haozhi Ma[3], Constantin M. Zohner[3], Thomas W. Crowther[3], Yuanyuan Huang[4,5], Xutong Wu[6], Fangli Wei[1]

1 State Key Laboratory of Urban and Regional Ecology, Research Center for Eco-Environmental Sciences, Chinese Academy of Sciences, Beijing, PR China.

2 College of Resources and Environment, University of Chinese Academy of Sciences, Beijing, PR China.

3 Institute of Integrative Biology, ETH Zurich (Swiss Federal Institute of Technology), Zurich, Switzerland.

4 Laboratoire des Sciences du Climat et de l'Environnement, LSCE/IPSL, CEA-CNRS-UVSQ, Université Paris-Saclay, Gif-sur-Yvette, France

5 Commonwealth Scientific and Industrial Research Organisation, Aspendale, Victoria, Australia

6 State Key Laboratory of Earth Surface Processes and Resource Ecology, Faculty of Geographical Science, Beijing Normal University, Beijing, PR China.

*Correspondence authors: fengxm@rcees.ac.cn

Abstract

To quantify the ecological consequences of recent nationwide restoration efforts in China, spatially-explicit information on forest biomass carbon stock changes over the past 20 years is critical. However, long-term biomass tracking at the national scale remains challenging as it requires continuous and high-resolution monitoring. Here, we characterize the changes in forests' above- and belowground biomass carbon (AGBC and BGBC) in China between 2002 and 2021 at 1 km spatial resolution by integrating multiple types of remote sensing observations with intensive field measurements through regression and machine learning approaches. On average, 8.6 ± 0.6 and 2.2 ± 0.1 PgC were stored in above- and belowground live forests in China. Over the last 20 years, the total forest biomass carbon pool in China has increased at a rate of 114.5 ± 16.3 TgC/yr (approximately 1.1%/yr). The most pronounced forest biomass carbon stock gains occurred in central to southern China, including the southern Loess Plateau, Qinling Mountains, southwest karsts and southeast forests. While the combined use of multi-source remote sensing data provides a powerful tool to assess the forest biomass carbon changes, future research is also needed to explore the drivers of the observed woody biomass trends, and to evaluate the degree to which biomass gains will translate into biodiverse, healthy ecosystems and thus are sustainable.

Key words: Aboveground biomass carbon pool; Belowground biomass carbon; Long-term continuous mapping; China

1 Introduction

Forest biomass carbon stock contributes to over 90% of the global vegetation biomass carbon pool (Ma et al., 2021). As a net outcome of carbon gains from photosynthesis and carbon losses from respiration, mortality and disturbances, forest biomass carbon stock (approximately 50% of biomass) is a critical indicator of ecosystem function and ecosystem services, such as carbon sequestration, wood production and resource allocation (Kumar and Mutanga, 2017). Accurate forest biomass carbon stock monitoring over space and time is thus essential for assessing ecosystem management strategies and mitigation policies (Kumar and Mutanga, 2017).

In recent decades, remote sensing tools have been integral in our efforts to map aboveground biomass (AGB) or carbon stock (AGBC). By combining satellite imagery (e.g., MODIS) and airborne LiDAR signals, forest cover and canopy height can be mapped across large spatial scales (Hu et al., 2016; Saatchi et al., 2011; Su et al., 2016; Tong et al., 2020; Xu et al., 2021). Apart from optical images and LiDAR signals, microwaves can provide more detailed insights into subcanopy forest structure and AGBC due to their ability to penetrate the canopy. Active microwave techniques, i.e., Synthetic Aperture Radar (SAR) backscatters, facilitate high-resolution (e.g., 100 m) AGB mapping, but the temporal coverage is limited (Cartus et al., 2012; Bouvet et al., 2018). Conversely, vegetation optical depth (VOD) retrieved from multiple passive microwave sensors can be used to produce long-term continuous AGB maps (Frappart et al., 2020; Liu et al., 2011; Liu et al., 2015), yet at a coarse spatial resolution (e.g., 0.25°). Because different remote sensing techniques have their advantages and pitfalls, combining

57 these techniques and complementing them with direct ground measurements is integral to

58 maximizing the accuracy and precision of biomass carbon estimations across space and time.

59 Another source of uncertainty in vegetation biomass carbon stocks is the extent of biomass that

60 is stored belowground as roots. While AGBC mapping is facilitated by a suite of emerging

61 remote sensing techniques, investigating the spatiotemporal variation in belowground biomass

62 carbon pool (BGBC) remains challenging despite the large contribution of roots to total carbon

63 storage (Huang et al., 2021; Ma et al., 2021). To map BGBC, the commonly-used approach is

64 to combine aboveground biomass information with vegetation type-specific ratios of BGB to

65 AGB (i.e., root-shoot ratio, or RSR) (Xu et al., 2021; Saatchi et al., 2011). Because field studies

66 indicate a near-linear relationship between log-transformed BGB and AGB (Enquist Brian and

67 Niklas Karl, 2002), BGB variations at large scales have often been approximated using this

68 relationship (Spawn et al., 2020). To capture the complex relationship between BGB and biotic

69 or abiotic variables (e.g., stand age, heat and water availability), machine learning algorithms

70 have been applied to map BGB (Huang et al., 2021) and root-mass fractions (Ma et al., 2021)

71 globally. However, the reference plots were unevenly distributed across the world, limited in

72 developing countries, leading to some uncertainties in BGB and BGBC estimation within those

73 regions (Huang et al., 2021).

74 China has been implementing national-scale afforestation and reforestation programs since the

75 late 1990s (Lu et al., 2018), promoting vegetation cover and carbon storage in the Loess Plateau

76 and the southwest karst regions, etc. (Chen et al., 2019a; Niu et al., 2019; Tong et al., 2018). A

77   spatial understanding of forest biomass trends can help evaluate the efficiency of ecological

78   restoration programs. High quality, high resolution and long-term continuous woody biomass

79   monitoring in China has remained challenging (Zhang et al., 2019; Huang et al., 2019).

80   In this study, by integrating multi-source remote sensing data with large quantities of plot

81   measurements, we produced 1 km resolution above- and belowground forest biomass carbon

82   pool maps for China during the past 20 years (2002–2021). This dataset could provide new

83   insights into forest carbon stock changes in China over the past two decades.

84   **2 Materials and methods**

85   To map above- and belowground forest biomass carbon stock in China during 2002–2021, we

86   1) calibrated a SAR-based high-resolution forest aboveground biomass map in China based on

87   massive field measurements of AGBC during 2011–2015; 2) extended the AGBC time series to

88   2002–2021 by referring to the tree and short vegetation cover retrieved from optical remote

89   sensing; 3) calibrated the AGBC time series in some specific areas using a long-term integrated

90   microwave-based VOD dataset; and 4) mapped forestlands' BGBC through a random forest

91   model developed based on the in-situ records in published literature. The basic procedure is

92   shown in Figure 1 and described below.
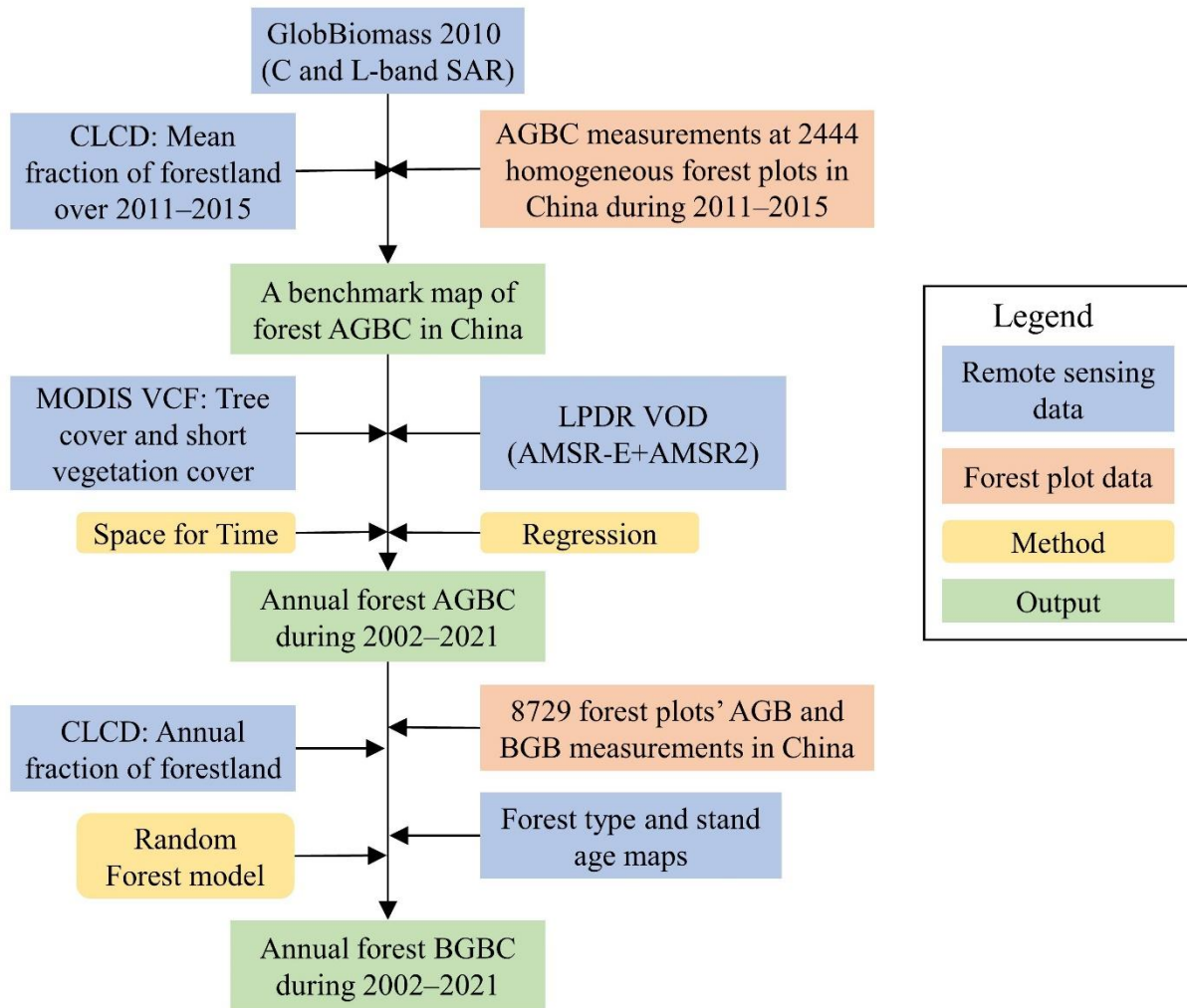
Figure 1. Workflow of forest biomass carbon pool monitoring in China during 2002–2021. AGBC, BGBC: aboveground and belowground biomass carbon; VCF: vegetation continuous fields; LPDR VOD: global land parameter data record- vegetation optical depth; CLCD: China Land Cover Dataset

**2.1 A benchmark map of forest aboveground biomass carbon (AGBC) in China**

By combining multiple satellite observations of SAR backscatter, including the L-band ALOS PALSAR and C-band Envisat ASAR around the year 2010, the first global high-resolution (100 m) forest AGB dataset, GlobBiomass 2010, was published through the European Space Agency (ESA)'s Data User Element project (Santoro et al., 2021), whose relative root mean square error

103 (RMSE) was below 30% (Mialon et al., 2020). Apart from GlobBiomass 2010, another high-

104 resolution (30 m) forest AGB for China was produced by relating the ICESat GLAS (LiDAR)-

105 derived footprint AGB to various variables derived from Landsat optical images (Huang et al.,

106 2019). Because the ICESat data in 2006 were applied as the training target of the random forest

107 model, Huang's dataset refers to the AGB status in 2006. According to a recent validation study,

108 GlobBiomass and Huang's AGB performed the best among all existing AGB datasets in China

109 (Chang et al., 2021). Mean forest canopy heights and tree coverage are also good indicators of

110 the spatial pattern of forest biomass. The high-resolution (30 m) forest canopy height map for

111 China was developed by interpolating the ICESat-2 and GEDI data in 2019 through a neural

112 network (Liu et al., 2022), while the tree cover map at the same resolution was derived from

113 cloud-free growing season composite Landsat 7 data in around 2010 (Hansen et al., 2013). We

114 resampled GlobBiomass from 100 m resolution (1/1125°) to 1/1200° (approximately 90 m),

115 and averaged Huang's AGB map, canopy height map and tree cover map to the same resolution.

116 A reviewable, consistent ecosystem carbon stock inventory was conducted in China between

117 2011 and 2015 (Tang et al., 2018). We requested the AGB carbon stock (AGBC) data at more

118 than 5,000 30×30 m sized forest plots from the authors. Due to the scale mismatch between the

119 maps of biomass, canopy height or tree cover and the field measurements, we dropped out the

120 data within the 1/1200° resolution grids in which the standard deviation of tree cover was

121 greater than 15%, according to (Chang et al., 2021), leaving 2444 homogeneous forest plots

122 remaining (see Figure 2 for the spatial distribution of these forest plots and Figure S1a~b for

123   the cumulative frequency curve and histogram of the AGBC records). The AGBC records in

124   these forest plots were further multiplied by the mean fraction of forestland over 2011–2015 in

125   the corresponding grid, which was computed from the annual 30 m resolution China Land

126   Cover Dataset (CLCD) (Yang and Huang, 2021). By comparison, GlobBiomass 2010 AGB

127   matches the best with the grid-scale forest AGBC derived from plot measurements, with a

128   correlation coefficient (CC) of 0.50, followed by tree cover (CC=0.42), the product of canopy

129   height and tree cover (CC=0.38), and finally the canopy height (0.27) and Huang's AGB (0.25).

130   Therefore, to obtain an improved benchmark map of forest AGBC in China for the period of

131   2011–2015, we chose the GlobBiomass 2010 dataset as our basis, and calibrated it against the

132   in-situ observation-based grid-scale forest AGBC. To build an equation for the calibration, we

133   divided the grid-scale AGBC values into 16 equidistant subranges (0~15, 15~30, …, 225~240

134   tC/ha), calculated the median of grid-scale AGBC values that are within each subrange, and

135   then the median of GlobBiomass AGB values in the corresponding grids. According to previous

136   studies, an exponential function would be suitable for calibrating the GlobBiomass map in a

137   region such as China (Mialon et al., 2020). After the calibration, we averaged the benchmark

138   AGBC map from 1/1200° to 1/120° (approximately 1 km) to further reduce the uncertainties.
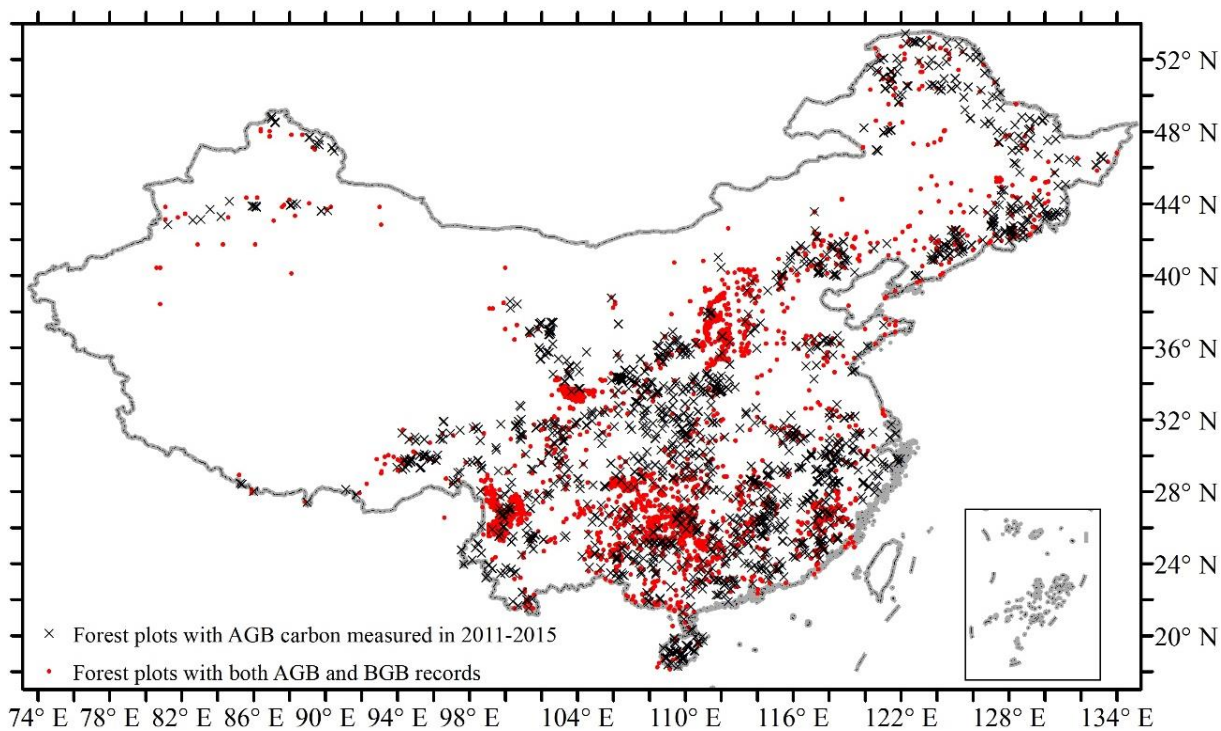
Figure 2. The spatial distribution of 1) 2444 homogeneous forest plots with aboveground

ground biomass carbon stock measured between 2011 and 2015; and 2) 8182 forest plots with

both above- and belowground biomass records collated in this study.

2.2 Temporally continuous forest AGBC mapping during 2002–2021

Because the benchmark AGBC was mapped based on SAR data, the spatial pattern accuracy is

guaranteed, but the temporal coverage is limited to just a few years. Hence, to create a forest

AGBC time series over the past 20 years, we integrated the benchmark AGBC with long-term

continuous optical and passive microwave remote sensing data.

The spatial resolution of optical remote sensing is higher, and is thus preferred in this study. By

adopting the MODIS vegetation continuous fields (VCF) data (MOD44B v061) which includes

three ground cover components: percent tree cover, percent non-tree vegetation (i.e., short

151 vegetation) cover, and percent non-vegetated (Dimiceli et al., 2022), we first calculated the

152 mean tree cover (hereinafter, TC_{mean}) and short vegetation cover (hereinafter SVC_{mean}) during

153 2011–2015, and resampled them from 250 m to 1/120°, the same resolution as the benchmark

154 AGBC map for 2011–2015. Because the canopy heights of trees are usually similar within a

155 small area, the regional AGBC per TC_{mean} can be assumed as the same, which is referred to as

156 the 'homogeneous assumption' hereinafter. Accordingly, for each grid, we searched the TC_{mean},

157 SVC_{mean} and AGBC within a 3×3 window (1/40°×1/40°), and then regressed the AGBC values

158 in 9 grids against both TC_{mean} (the primary, or key predictor of AGBC) and SVC_{mean} (assumed

159 as a supplementary predictor) linearly. Specifically, when the regression coefficient of SVC_{mean}

160 was negative or the fitting efficiency was low ($R^2<0.5$; significance p-value>0.05), we excluded

161 the supplementary predictor from the regression, only exploring the linear relationship between

162 TC_{mean} and AGBC. Afterwards, if the regression between TC_{mean} and AGBC was still invalid,

163 we enlarged the searching window size to 5×5, then 7×7, and finally 9×9, until the regression

164 as well as the coefficients became valid. Then, the grid annual AGBC from 2002 to 2021 can

165 be estimated from the TC or both TC and SVC in each year, following the regression results. If

166 the regression failed even if the window size reached 9×9, we stopped expanding the searching

167 window to avoid the 'homogeneous assumption' being invalid. In those grids, following a

168 previous study (Xu et al., 2021), we divided the estimated AGBC by the TC_{mean} during 2011–

169 2015 and then multiplied the TC in each year to obtain the AGBC time series. The above

170 method utilized spatial information to estimate the temporal variation, and can thus be referred

171 to as the 'space for time' method.

172 Long-term continuous microwave VOD can also reflect forest biomass changes, although the

173 relationship was nonlinear (Jackson and Schmugge, 1991; O'neill et al., 2021; Liu et al., 2015;

174 Wigneron et al., 1995). We selected the global land parameter data record (LPDR) v3 0.25°

175 resolution VOD product, which was generated using similar calibrated, X-band brightness

176 temperature retrieved from the Advanced Microwave Scanning Radiometer (AMSR-E) and the

177 Advanced Microwave Scanning Radiometer 2 (AMSR2) (Du et al., 2017). As revealed by a

178 recent evaluation study, LPDR VOD is better correlated with AGB than other long-term VOD

179 products, especially in less-vegetated areas (Li et al., 2021). Because X-band VODs are still

180 more sensitive to canopy cover than stem biomass and there is a data gap between October 2010

181 and June 2011, while the plot investigations were all conducted in summers (Tang et al., 2018),

182 we averaged the VOD data from mid-July (the 206th day) until the end of September (the 274th

183 day) in each year to represent the annual AGB status. We also aggregated the benchmark AGBC

184 map as well as the VCF data (TC_{mean} and SVC_{mean}) to 0.25° resolution. After each round of

185 searching, we applied the shape language modelling algorithm (D'errico, 2022) to fit the

186 nonlinear but monotonous relationship between AGBC and VOD values within the searching

187 window, and then fitted the bivariate linear regression between AGBC and VCF. If the nonlinear

188 regression between AGBC and VOD is valid and the R^2 is superior to the regression between

189 AGBC and VCF data, LPDR VOD data is expected to outperform VCF in predicting the inter-

190 annual AGBC changes in the corresponding 0.25° grid. Therefore, in these areas, we calibrated

191 the VCF-derived high (1/120°) resolution annual AGBC by incorporating the ratio between the

192 VOD-derived 0.25° AGBC and the aggregated VCF-derived AGBC in that year.

2.3 Forest belowground biomass carbon (BGBC) mapping during 2002–2021

This study mapped belowground forest biomass carbon (BGBC) following the random forest (RF) model approach (Huang et al., 2021). To reveal forests' above- and belowground biomass allocation rules in China, this study collated both AGB and BGB records at 8729 forest plots throughout China, which were obtained using allometric equations or clear-cutting methods from published papers, including (Luo, 1996), (Luo et al., 2014), (Guo and Ren, 2014), (Wang et al., 2014). Because forest stand age and tree species (forest type) information are also available at 8182 plots, while the climatic backgrounds are available from the WorldClim v2.1 dataset (Fick and Hijmans, 2017), forest plots' AGB, forest type (hereinafter FOR_T), stand age, mean annual temperature (MAT), temperature seasonality (standard deviation of monthly temperature×100, abbreviated as Tsea), mean annual precipitation (MAP) and precipitation seasonality (coefficient of variation of monthly precipitation, Psea) were applied as predictors of forest plots' BGB. For simplicity, we distinguished all forests into 5 types: evergreen broadleaf forest (EBF), deciduous broadleaf forest (DBF), evergreen needleleaf forest (ENF), deciduous needleleaf forest (DNF), and mixed forest (MF). Using the data records at these 8182 plots (see Figure 2 for the locations of these forest plots and Figure S1c~f for the cumulative frequency curves and histograms of the AGB and BGB data), we trained ten-fold RF models using MATLAB R2021a[®]. The number of regression trees was set to 500.

Because the 1/120° resolution grids where forest AGBC data were available are often mixed with forestland and some other land cover types, e.g., water bodies, bare ground, croplands, we

converted the annual grid-average AGBC into the AGBC per area forestland by incorporating

the annual fraction of forestland computed from the CLCD at 30 m resolution. Considering the

potential uncertainties in the forestland fraction as well as the inclusion of shrub or herbaceous

plant AGB in the SAR-derived AGB, we only calculated the annual AGBC per area forestland

in grids that were dominated by forestland (forestland fractions were consistently over 50%).

In these forestland grids, we simulated the forest BGBC per area forestland during 2002–2021

by inputting the estimated annual AGB (approximately 2 times of the AGBC) per forestland,

annual forest type map derived from ESA CCI's land cover classification dataset (Li et al.,

2018), forest stand age (Besnard et al., 2021) and climatic background variables into the RF

model. Afterwards, we multiplied the simulation results in every forestland grid with the annual

forestland fractions to obtain the forests' BGB and BGBC (0.5×BGB) time series. Finally, for

grids with forests but are not dominated by forestlands, we sequentially searched for at least

five valid RSR values (the ratio of forests' BGBC to AGBC) nearby (Chen et al., 2019b), and

then multiplied the annual forest AGBC in the grid with the median of nearby RSR values in

each year to estimate the annual forest BGBC.

2.4 Evaluation and assessment

We compared the inter-annual trend of forest biomass carbon calculated in this study against

that of existing global/regional long-term woody biomass datasets, including the well-received

global long-term terrestrial biomass data between 1993–2012, which was developed mainly

based on a long-term integrated VOD dataset (Liu et al., 2015), as well as an updated woody

233 biomass dataset covering 2001–2019 whose long time series was derived from optical remote

234 sensing data (i.e., MODIS VCF dataset) (Xu et al., 2021).

235 To justify the random forest models for BGBC predictions, we drew partial dependence plots

236 (PDPs) in MATLAB R2021a® to show the marginal effect that one predictor has on the training

237 target (e.g., BGB at forest plots) (Hastie et al., 2009). Here, for each predictor, we excluded the

238 extreme values (the lowest 1% and the highest 1%) before calculating the corresponding PDP

239 to avoid roughly extending the PDP lines to data-scarce areas. Ten-fold RF trainings were also

240 performed to derive the mean PDP values as well as the standard deviations.

3 Results and discussion

3.1 Evaluation of forests' AGBC and BGBC estimation

243 First, according to Figure 3a, an exponential function: $y=1.63 \times x^{0.73}$ can fit the relationship

244 between the actual grid-scale forest AGBC over 2011–2015 (y) and the AGB values predicted

245 by GlobBiomass 2010 (x). Hence, this function was applied to derive the benchmark map of

246 forest AGBC across China.

247 Second, when using the spatial information of tree cover and short vegetation cover to estimate

248 the temporal variation of AGBC in each grid, the spatial searching window was at its minimum

249 of 3×3 in most (53%) grids with forests. Across China, the temporal extension of AGBC in only

250 15% of all grids with forest cannot be achieved even when the searching window was enlarged

251 to 9×9 (Figure 3b).

252　Next, as shown in Figure 3c and 3d, the grids where LPDR X-band VOD performed better than

253　MODIS VCF in predicting the temporal change in forest AGBC are usually located in regions

254　with low tree cover. These grids account for just 10.4% of all grids with forests, and may suffer

255　from high uncertainty within the optical-based variation in tree cover. Therefore, microwave-

256　based VOD is supposed to be more suitable for estimating the forests' AGBC changes in these

257　regions.
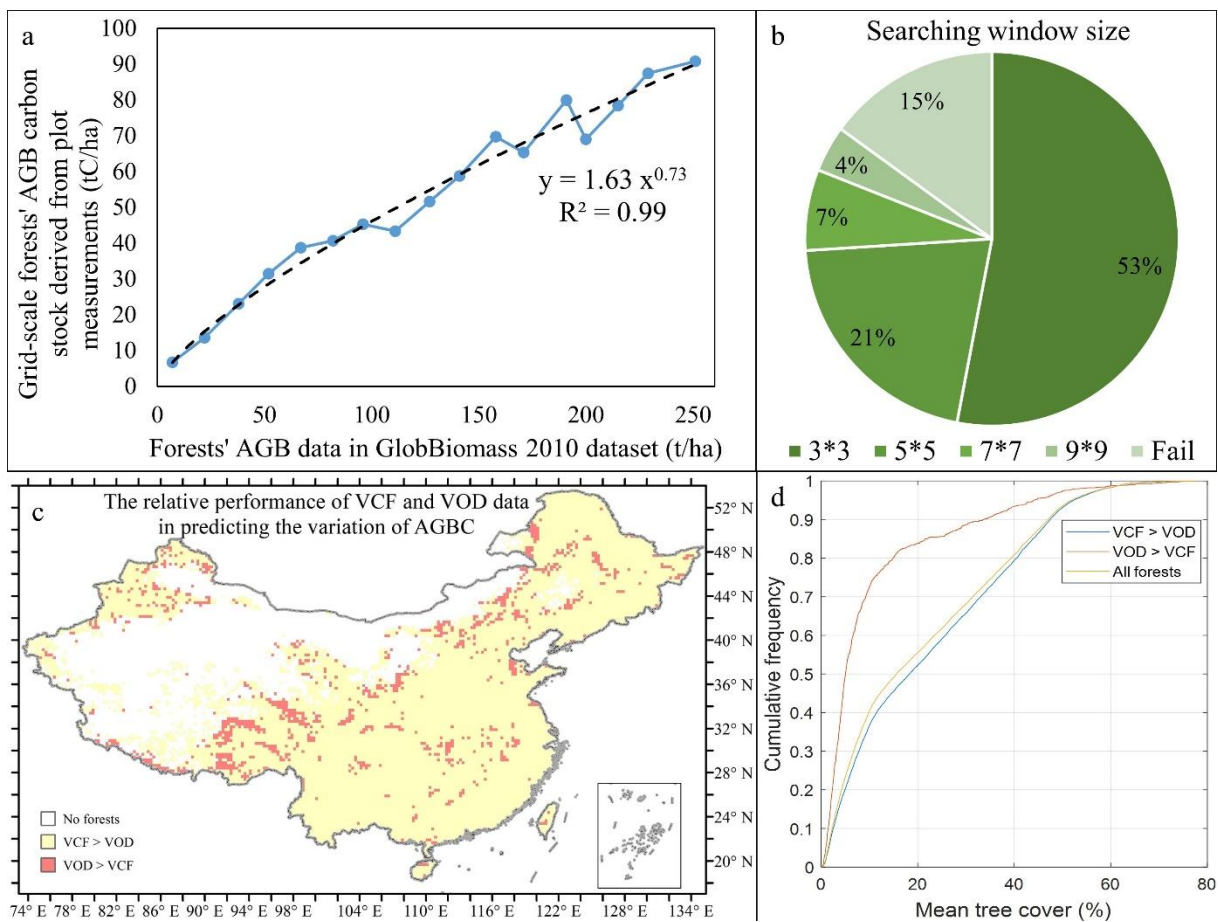
258

259　Figure 3. Evaluation of the forest AGBC and BGBC mapping in this study. (a) The regression

260　relationship between the grid-scale forest AGB carbon stock derived from plot measurements

261　during 2011–2015 and the GlobBiomass AGB dataset for 2010; (b) the minimum searching

262　window sizes of every 1/120° grid when the spatial variation in MODIS VCF was applied as

263   the predictor of AGBC changes; (c) the spatial pattern of the relative performances of MODIS

264   VCF and LPDR VOD data in predicting the variation in AGBC; (d) comparison of the mean

265   tree cover between the grids where VOD data were more suitable for predicting the variation

266   of AGBC and the grids where VCF data were the better predictor.

267   The RF model designed for forest plot BGB estimation (see section 2.3) achieved a predictive

268   R^2 of 0.89±0.02, while the RMSE was 6.3±0.5 t/ha. AGB explained 53% of the variation in

269   BGB among different plots. Long-term climate backgrounds, i.e., mean annual temperature,

270   temperature seasonality, annual precipitation and precipitation seasonality accounted for 8%,

271   6%, 8% and 7%, respectively. Forest type and stand age also contributed 12% and 8% to the

272   training efficiency, indicating that the effects of these factors are nonnegligible. The selection

273   of predictors of BGB basically followed the existing knowledge (Huang et al., 2021), and the

274   seasonality of temperature and precipitation made sense in the prediction (see Text S1). On the

275   other hand, although previous studies incorporated many edaphic factors as predictors of BGB

276   (Huang et al., 2021), by comparing the training efficiencies when whether these edaphic factors

277   are incorporated or not, we could justify the reasonability of our simplified set of predictors

278   (Text S1).

279   According to the collected woody plots' data, AGB is a key driver of BGB (Figure 4). Yet, RSR

280   changes among different forest growth stages, decreasing in general as reported (Mokany et al.,

281   2006). The overall negative impact of mean temperature on BGB or RSR agrees with the

282   mechanism that higher heat promotes nutrient accessibility (Luo et al., 2012; Ma et al., 2021),

283 and increases the turnover rates of roots at a higher magnitude than stems (Reich et al., 2014).

284 The 'U-shaped' relationship between precipitation and belowground biomass allocation follows

285 the 'optimal biomass allocation' theory, because arid climates promote root extension, yet too

286 heavy rainfall reduces nutrient availability through leaching and dilution effects (Luo et al.,

287 2012). Other factors, including temperature seasonality, precipitation seasonality and forest

288 type, have supplementary effects on biomass allocation (Figure S2).

289
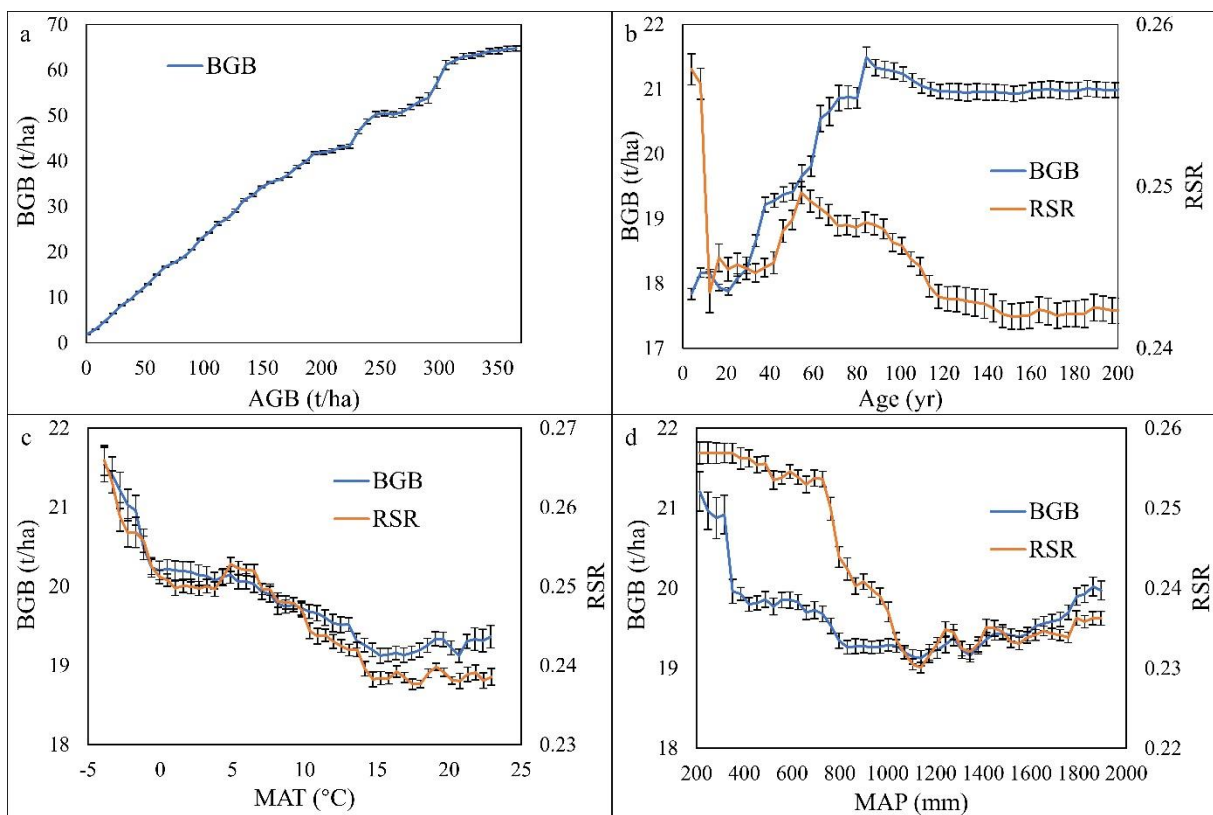
290 **Figure 4.** Influence of key factors on forest belowground biomass (BGB) and root-shoot ratio

291 (RSR) in China. Subfigures (a~d) show partial influences of (a) AGB; (b) stand age; (c) MAT

292 and (d) MAP on BGB and RSR values of all forest plots. The error bars represent the standard

293 deviations of the ten-fold trainings. We did not draw the PDP for the impact of AGB on RSR,

294 since the dividend of RSR calculation is AGB.

3.2 Forest biomass carbon pool, allocation and change in China

Between 2002 to 2021, the forest above- and belowground biomass carbon (AGBC and BGBC) pools in China were 8.6 ± 0.6 and 2.2 ± 0.1 PgC, respectively (Table 1). The mean RSR for all forests was 0.25, basically equal to the global average (Huang et al., 2021). Separated by forest type, evergreen conifer forests (ENF) occupy the highest biomass carbon pool per unit area, mainly because ENF are mainly located in southwestern China and are more mature and natural (Yu et al., 2020; Zhang et al., 2017). Deciduous forests (DBF & DNF) in northern China (see Figure S3 for the distribution of different forest ecosystems) harbor less biomass carbon but higher BGBC (Figure 5a), which can be attributed to the higher RSR values (Table 1).

The forest biomass carbon stock in China increased at an average rate of 114.5 ± 16.3 TgC/yr (p<0.01) during 2002–2021, and the annual biomass carbon gains were the greatest from 2014 to 2015, reaching 736 TgC (Figure 5b). Changes in AGB and BGB accounted for 81.9% and 18.1%, respectively, of the forest carbon stock gains over the past 20 years.

Our estimates of the forest biomass carbon pool, forest RSR and the recent inter-annual trend of forest biomass carbon are generally consistent with previous estimates based on massive field investigations (Table 1).

Table 1. Agreement of the estimated various forest RSR and the trend of forest biomass carbon in China with existing studies.

Variables	Our estimate	Previous estimates	Reference
Forests' AGBC	8.6 ± 0.6 (2002–2021) 8.7 ± 0.3 (2011–2015)	8.4 ± 1.6 (2011–2015)	(Tang et al., 2018)
Forests' BGBC	2.2 ± 0.1 (2002–2021)	2.1 ± 0.4 (2011–2015)	

|	2.2 ± 0.1 (2011–2015)		
EBF's RSR	0.27±0.07	0.22±0.11	
DBF's RSR	0.31±0.05	0.28±0.15	(Tang et al., 2018)
ENF's RSR	0.22±0.04	0.24±0.11	
DNF's RSR	0.29±0.10	0.31±0.13	
Annual forest carbon stock increase	114.5 ± 16.3 TgC/yr (2002–2021)	116.7 TgC/yr (2000–2010)	(Fang et al., 2018)
	105.1 ± 42.2 TgC/yr (2002–2010)		
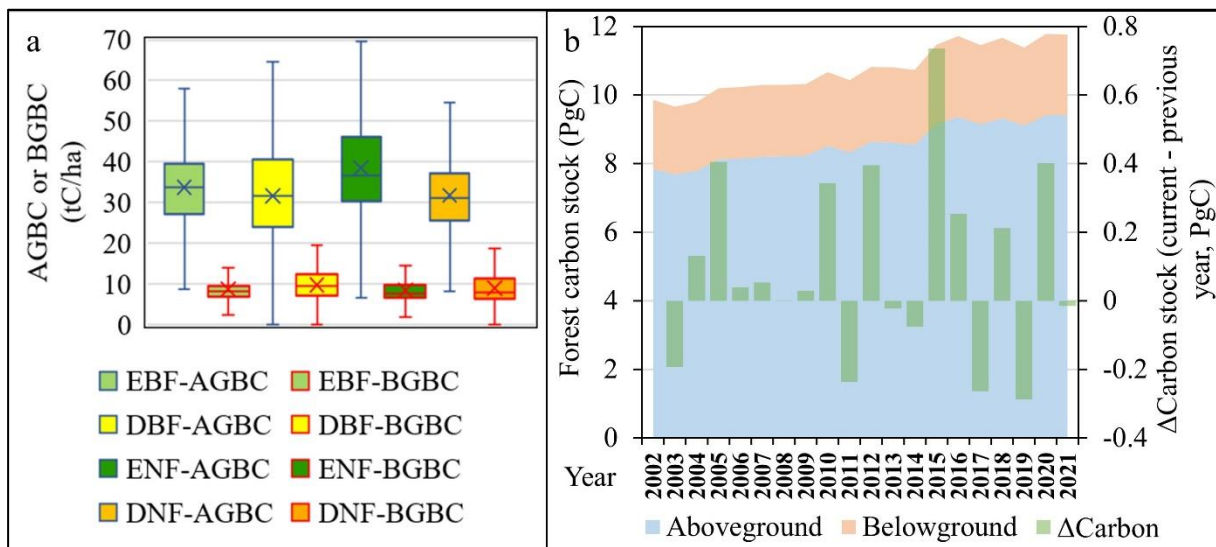
Figure 5. Forest biomass allocation and biomass change in China during 2002–2021: (a) aboveground biomass carbon (AGBC) and belowground biomass carbon (BGBC) density of different forest ecosystems in China; (b) the inter-annual changes of forest AGBC and BGBC in China. Total forest biomass carbon stock changes from the previous to the current year are represented by green columns.

3.3 Spatial pattern of the forest biomass carbon stock trend in China

The highest forest biomass carbon pools during 2002–2021 were observed in northeastern and southwestern China, especially southern Tibet. Forest biomass carbon stocks were also high in the natural or semi-natural forests in the Qinling Mountains, Hengduan Mountains, Hainan and Taiwan (Figure 6a). Above- and belowground forest biomass allocation varies significantly

19

among regions. RSR is highest in northeastern deciduous conifer forests and northern China's

deciduous broadleaf forests but low in southern China (Figure 6b). The strongest forest biomass

carbon increases were found in central to southern China, including the Loess Plateau, Qinling

Mountains, southwest karst region and southeastern forests. Slight declines in forest biomass

carbon only occurred in some mature and natural forests, e.g., those in the Greater Khingan

Mountain, Hengduan Mountains and South Tibet (Figure 6c). A total of 40.3% of all forests in

China showed significant biomass carbon stock gains over the past 20 years, whereas only 3.3%

of forests experienced significant biomass carbon losses (Figure 6d).
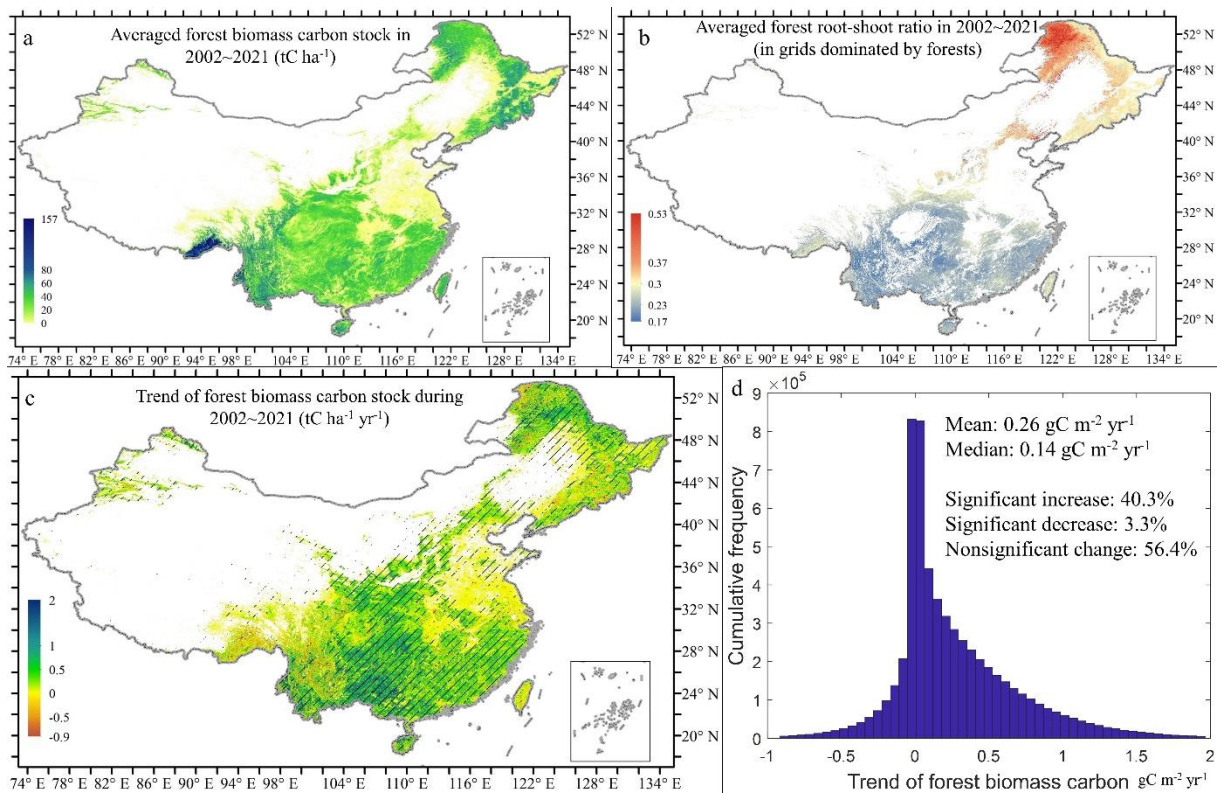
Figure 6. Maps of forest biomass carbon pool, allocation and trend in China during 2002–2021.
(a) Spatial pattern of the forest biomass carbon pool in China; (b) all forestland pixels' RSR; (c)
map of the forest biomass carbon stock trend from 2002 to 2021, with shaded areas representing
statistically significant trends at the 95% confidence level; (d) histogram and basic statistics of

337   all forest biomass carbon stock trend.

4 Discussion

4.1 Comparison of the estimated forest biomass carbon pool change in this study against the existing datasets

341   Although with potential overestimation, the inter-annual variation in forest AGBC in China

342   according to Liu et al. (2015) and that of total biomass carbon according to Xu et al. (2021) are

343   both highly correlated with our results (R^2= 0.65 and 0.88). Liu et al. predicted a forest AGBC

344   increase rate of 102.2 ± 35.8 Tg/yr (p<0.01), slightly higher than our estimate of 80.8 ± 25.1

345   Tg/yr during 2002–2012; while Xu et al. indicated a biomass carbon stock trend of 99.4 ± 23.2

346   Tg/yr (p<0.01) from 2002 to 2019, slightly lower than the rate of 115.6 ± 20.2 Tg/yr in this

347   study (Figure 7a~b). The spatial maps of the forest biomass carbon trends estimated by Xu et

348   al. and Liu et al. were slightly patchy (Figure 7c~d). Compared to this study, the two existing

349   datasets (i.e., Liu et al. (2015) and Xu et al. (2021)'s datasets) predicted higher biomass carbon

350   stock trends in the Qinling Mountains and the mature deciduous conifer forests in northeast

351   China. Meanwhile, they predicted lower carbon sinks in southern China (Figure 7c~f), where

352   reforestation and forest management-induced short term extensive carbon uptake (Tong et al.,

353   2020) have been confirmed by atmospheric inversions (Wang et al., 2020; Yang et al., 2021).

354   Finally, by comparing Figure 7e and 7f, we could also notice that the hotspot of forest biomass

355   carbon gains has moved from the Loess Plateau over the first decade of our study period (2002–

356   2012) to southern China (e.g., Guangxi Province) later. This change was probably due to the

large-scale implementation of the 'Grain for Green' project on the Loess Plateau (Liu et al., 2020; Wu et al., 2019) before 2012, and the massive plantation of fast-growing trees in southern China after 2010 (Tong et al., 2020).
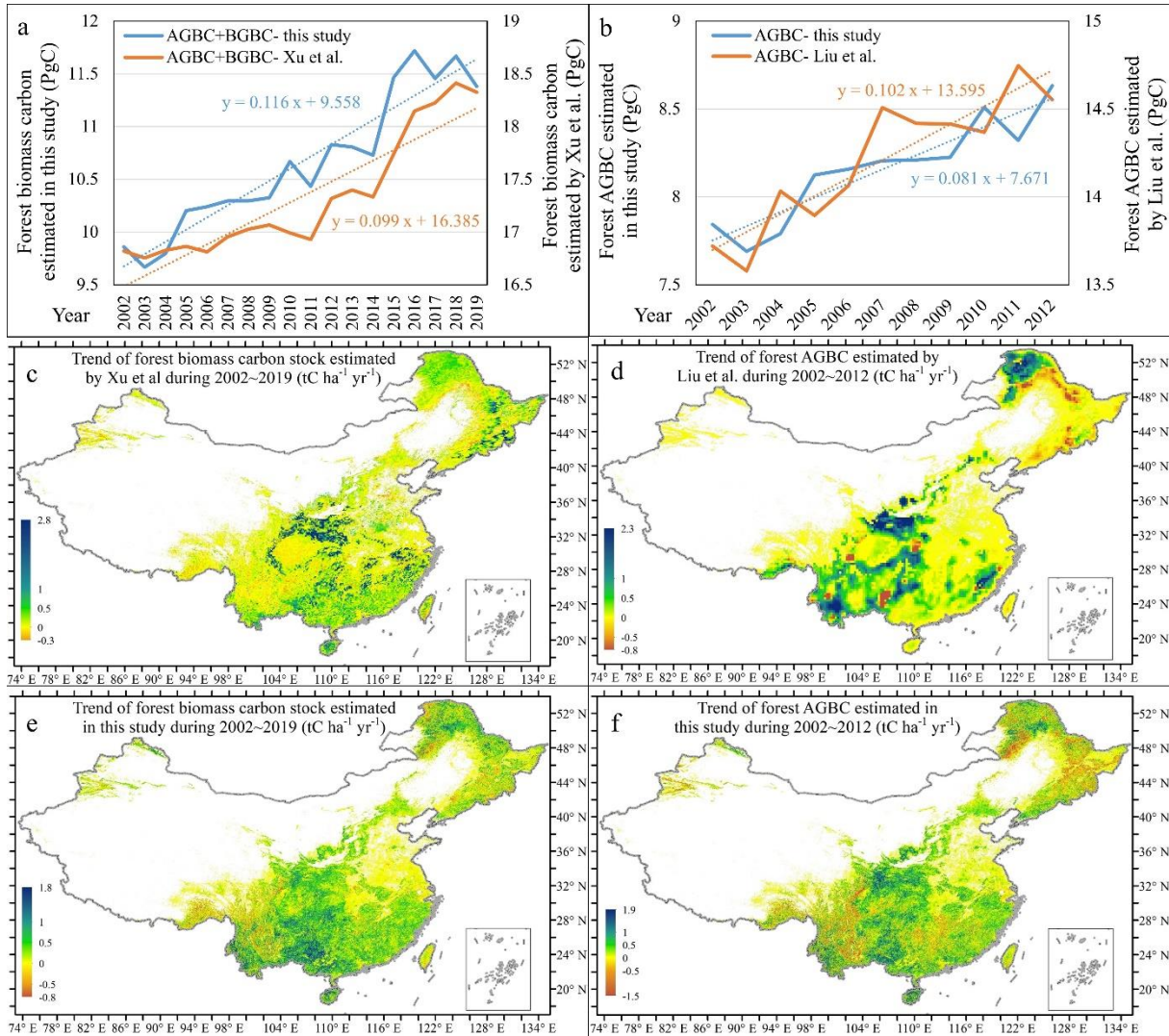
Figure 7. Comparison of the estimated forest biomass carbon pool change in this study against two existing datasets. (a) Comparison of the inter-annual variation of forest biomass carbon in this study against the estimate by Xu et al. during 2002–2019; (b) comparison of the inter-annual variation of forest AGBC calculated in this study against the estimate by Liu et al. over 2002–2012; (c) map of the inter-annual trend of forest biomass carbon stock in China during

22

366 2003–2019 according to Xu et al; (d) map of the forest AGBC trend in China during 2003–2012

367 according to Liu et al; (e) map of the estimated trend of forest biomass carbon stock over 2002–

368 2019 in this study; (f) map of the estimated forest AGBC trend over 2002–2012 in this study.

4.2 Some uncertainties of the forest biomass carbon dataset and future prospects

370 During benchmark AGBC mapping, we converted the in-situ AGBC data at forest plots into the

371 grid-scale average AGBC by multiplying by the fraction of forestland during the time period of

372 field investigation. Considering the overall high-quality of the China's land-use/cover datasets

373 developed via human–computer interactive interpretation of Landsat images (Liu et al., 2014;

374 Yang and Huang, 2021), and that the producer's accuracy (PA) and user's accuracy (UA) for

375 forestland classification in the CLCD dataset used in this study were 73% and 85% respectively,

376 the errors within the benchmark AGBC mapping induced by the scale conversion based on the

377 forestland area fraction were generally limited.

378 The variation in climatic conditions in the short term may have subtle influences on that in the

379 BGB, but explicit knowledge on this effect is lacking. Instead, woody vegetation BGB is much

380 more driven by AGB (vegetation density), as indicated by the very strong relationship between

381 BGB and AGB ($R^2 \geq 0.85$). Moreover, the long-term climatic background is expected to have a

382 stronger influence on the RSR of perennial woody plants than the meteorological conditions in

383 only a few years, since above- and belowground biomass allocation is the result of plants' long-

384 term adjustment to the environment (Qi et al., 2019). Therefore, it is reasonable not to consider

385 the influence of the specific climatic conditions in a year on the variation in BGB.

386   In the near future, P-band microwave sensors, which have higher penetrability into the canopy

387   than L-band microwaves, will further improve AGB mapping. For example, BIOMASS, a fully

388   polarimetric P-band SAR, is scheduled to be launched in 2022 (Le Toan et al., 2011). Therefore,

389   in the future the relationship between P-band microwave retrievals and biomass should be

390   addressed, as well as the calibration of historical AGB datasets (e.g., the long-term AGB dataset

391   in this study) against the P-band SAR-based AGB benchmark map to extend the time series. In

392   addition, an inter-calibration between the AMSR-E-based VOD and the AMSR2-based VOD

393   will further reduce the potential bias within the long-term integrated VOD datasets (Wang et al.,

394   2021a; Wang et al., 2021b). On the other hand, more in-situ AGB and BGB measurements in

395   larger plots are needed to further improve the estimation of belowground biomass allocation.

396   **Data availability**

397   Annual forest above- and belowground biomass maps in China between 2002 and 2021 are now

398   available at: https://doi.org/10.6084/m9.figshare.21931161.v1. This dataset will also be

399   available on the National Tibetan Plateau/Third Pole Environment Data Center and PANGAEA

400   soon (under checking now). Other open datasets that made this research possible and the related

401   references are attached in Supplementary Information- Text S2.

406   for sharing his forest aboveground biomass map.

Conflict of interests

408   The authors declare no conflict of interest.

Credit author statement

410   Y.C designed and conducted the research. B.F and X.F funded the research. Y.Z wrote the draft

411   of the manuscript; X.F and all other authors read and revised the manuscript.

References

413   Besnard, S., Koirala, S., Santoro, M., Weber, U., Nelson, J., Gütter, J., Herault, B., Kassi, J., N'Guessan, A., Neigh,
414   C., Poulter, B., Zhang, T., and Carvalhais, N.: Mapping global forest age from forest inventories, biomass and
415   climate data, Earth Syst. Sci. Data, 13, 4881-4896, https://doi.org/10.5194/essd-13-4881-2021, 2021.

416   Bouvet, A., Mermoz, S., Le Toan, T., Villard, L., Mathieu, R., Naidoo, L., and Asner, G. P.: An above-ground
417   biomass map of African savannahs and woodlands at 25m resolution derived from ALOS PALSAR, Remote Sens.
418   Environ., 206, 156-173, https://doi.org/10.1016/j.rse.2017.12.030, 2018.

419   Cartus, O., Santoro, M., and Kellndorfer, J.: Mapping forest aboveground biomass in the Northeastern United
420   States with ALOS PALSAR dual-polarization L-band, Remote Sens. Environ., 124, 466-478,
421   https://doi.org/10.1016/j.rse.2012.05.029, 2012.

422   Chang, Z., Hobeichi, S., Wang, Y.-P., Tang, X., Abramowitz, G., Chen, Y., Cao, N., Yu, M., Huang, H., Zhou, G.,
423   Wang, G., Ma, K., Du, S., Li, S., Han, S., Ma, Y., Wigneron, J.-P., Fan, L., Saatchi, S. S., and Yan, J.: New Forest
424   Aboveground Biomass Maps of China Integrating Multiple Datasets, Remote Sens., 13,
425   https://doi.org/10.3390/rs13152892, 2021.

426   Chen, C., Park, T., Wang, X., Piao, S., Xu, B., Chaturvedi, R. K., Fuchs, R., Brovkin, V., Ciais, P., Fensholt, R.,
427   Tømmervik, H., Bala, G., Zhu, Z., Nemani, R. R., and Myneni, R. B.: China and India lead in greening of the
428   world through land-use management, Nat. Sustain., 2, 122-129,
429   https://doi.org/10.1029/2018EF00089010.1038/s41893-019-0220-7, 2019a.

430   Chen, Y., Feng, X., Fu, B., Shi, W., Yin, L., and Lv, Y.: Recent Global Cropland Water Consumption Constrained
431   by Observations, Water Resour. Res., 55, 3708-3738, http://doi.org/10.1029/2018WR023573, 2019b.

432   D'Errico, J.: SLM - Shape Language Modeling MATLAB Central File Exchange [code], 2022.

433   DiMiceli, C., Sohlberg, R., and Townshend, J.: MODIS/Terra Vegetation Continuous Fields Yearly L3 Global
434   250m SIN Grid V061. [dataset], https://doi.org/10.5067/MODIS/MOD44B.061, 2022.

Du, J., Kimball, J. S., Jones, L. A., Kim, Y., Glassy, J., and Watts, J. D.: A global satellite environmental data record derived from AMSR-E and AMSR2 microwave Earth observations, Earth Syst. Sci. Data, 9, 791-808, https://doi.org/10.5194/essd-9-791-2017, 2017.

Enquist Brian, J. and Niklas Karl, J.: Global Allocation Rules for Patterns of Biomass Partitioning in Seed Plants, Science, 295, 1517-1520, https://doi.org/10.1029/2018EF00089010.1126/science.1066360, 2002.

Fang, J., Yu, G., Liu, L., Hu, S., and Chapin, F. S.: Climate change, human impacts, and carbon sequestration in China, P. Natl. Acad. Sci. USA, 115, 4015, https://doi.org/10.1029/2018EF00089010.1073/pnas.1700304115, 2018.

Fick, S. E. and Hijmans, R. J.: WorldClim 2: new 1-km spatial resolution climate surfaces for global land areas, Int. J. Climatol., 37, 4302-4315, https://doi.org/10.1029/2018EF00089010.1002/joc.5086, 2017.

Frappart, F., Wigneron, J.-P., Li, X., Liu, X., Al-Yaari, A., Fan, L., Wang, M., Moisy, C., Le Masson, E., Aoulad Lafkih, Z., Vallé, C., Ygorra, B., and Baghdadi, N.: Global Monitoring of the Vegetation Dynamics from the Vegetation Optical Depth (VOD): A Review, Remote Sens., 12, https://doi.org/10.1029/2018EF00089010.3390/rs12182915, 2020.

Guo, Q. and Ren, H.: Productivity as related to diversity and age in planted versus natural forests, Global Ecol. Biogeogr., 23, 1461-1471, https://doi.org/10.1111/geb.12238, 2014.

Hansen, M. C., Potapov, P. V., Moore, R., Hancher, M., Turubanova, S. A., Tyukavina, A., Thau, D., Stehman, S. V., Goetz, S. J., Loveland, T. R., Kommareddy, A., Egorov, A., Chini, L., Justice, C. O., and Townshend, J. R. G.: High-Resolution Global Maps of 21st-Century Forest Cover Change, Science, 342, 850-853, https://doi.org/10.1126/science.1244693, 2013.

Hastie, T., Tibshirani, R., and Friedman, J.: The Elements of Statistical Learning Data Mining, Inference, and Prediction, Second Edition, Section 10.13.2, Springer2009.

Hu, T., Su, Y., Xue, B., Liu, J., Zhao, X., Fang, J., and Guo, Q.: Mapping Global Forest Aboveground Biomass with Spaceborne LiDAR, Optical Imagery, and Forest Inventory Data, Remote Sens., 8, https://doi.org/10.1029/2018EF00089010.3390/rs8070565, 2016.

Huang, H., Liu, C., Wang, X., Zhou, X., and Gong, P.: Integration of multi-resource remotely sensed data and allometric models for forest aboveground biomass estimation in China, Remote. Sens. Environ., 221, 225-234, https://doi.org/10.1016/j.rse.2018.11.017, 2019.

Huang, Y., Ciais, P., Santoro, M., Makowski, D., Chave, J., Schepaschenko, D., Abramoff, R. Z., Goll, D. S., Yang, H., Chen, Y., Wei, W., and Piao, S.: A global map of root biomass across the world's forests, Earth Syst. Sci. Data, 13, 4263-4274, https://doi.org/10.1029/2018EF00089010.5194/essd-13-4263-2021, 2021.

Jackson, T. J. and Schmugge, T. J.: Vegetation effects on the microwave emission of soils, Remote. Sens. Environ., 36, 203-212, https://doi.org/10.1016/0034-4257(91)90057-D, 1991.

Kumar, L. and Mutanga, O.: Remote Sensing of Above-Ground Biomass, Remote Sens., 9, https://doi.org/10.1029/2018EF00089010.3390/rs9090935, 2017.

Le Toan, T., Quegan, S., Davidson, M. W. J., Balzter, H., Paillou, P., Papathanassiou, K., Plummer, S., Rocca, F., Saatchi, S., Shugart, H., and Ulander, L.: The BIOMASS mission: Mapping global forest biomass to better understand the terrestrial carbon cycle, Remote. Sens. Environ., 115, 2850-2860, https://doi.org/10.1016/j.rse.2011.03.020, 2011.

Li, W., MacBean, N., Ciais, P., Defourny, P., Lamarche, C., Bontemps, S., Houghton, R. A., and Peng, S.: Gross and net land cover changes in the main plant functional types derived from the annual ESA CCI land cover maps (1992–2015), Earth Syst. Sci. Data, 10, 219-234, https://doi.org/10.1029/2018EF00089010.5194/essd-10-219-2018, 2018.

Li, X., Wigneron, J.-P., Frappart, F., Fan, L., Ciais, P., Fensholt, R., Entekhabi, D., Brandt, M., Konings, A. G., Liu, X., Wang, M., Al-Yaari, A., and Moisy, C.: Global-scale assessment and inter-comparison of recently developed/reprocessed microwave satellite vegetation optical depth products, Remote. Sens. Environ., 253, 112208, https://doi.org/10.1016/j.rse.2020.112208, 2021.

Liu, J., Kuang, W., Zhang, Z., Xu, X., Qin, Y., Ning, J., Zhou, W., Zhang, S., Li, R., Yan, C., Wu, S., Shi, X., Jiang, N., Yu, D., Pan, X., and Chi, W.: Spatiotemporal characteristics, patterns and causes of land use changes in China since the late 1980s, Dili Xuebao/Acta Geogr. Sin., 69, 3-14, https://doi.org/10.11821/dlxb201401001, 2014.

Liu, X., Su, Y., Hu, T., Yang, Q., Liu, B., Deng, Y., Tang, H., Tang, Z., Fang, J., and Guo, Q.: Neural network guided interpolation for mapping canopy height of China's forests by integrating GEDI and ICESat-2 data, Remote. Sens. Environ., 269, 112844, https://doi.org/10.1016/j.rse.2021.112844, 2022.

Liu, Y. Y., de Jeu, R. A. M., McCabe, M. F., Evans, J. P., and van Dijk, A. I. J. M.: Global long-term passive microwave satellite-based retrievals of vegetation optical depth, Geophys. Res. Lett., 38, https://doi.org/10.1029/2011GL048684, 2011.

Liu, Y. Y., van Dijk, A. I. J. M., de Jeu, R. A. M., Canadell, J. G., McCabe, M. F., Evans, J. P., and Wang, G.: Recent reversal in loss of global terrestrial biomass, Nat. Clim. Change, 5, 470-474, https://doi.org/10.1029/2018EF00089010.1038/nclimate2581, 2015.

Liu, Z., Wang, J., Wang, X., and Wang, Y.: Understanding the impacts of 'Grain for Green' land management practice on land greening dynamics over the Loess Plateau of China, Land Use Policy, 99, 105084, https://doi.org/10.1016/j.landusepol.2020.105084, 2020.

Lu, F., Hu, H., Sun, W., Zhu, J., Liu, G., Zhou, W., Zhang, Q., Shi, P., Liu, X., Wu, X., Zhang, L., Wei, X., Dai, L., Zhang, K., Sun, Y., Xue, S., Zhang, W., Xiong, D., Deng, L., Liu, B., Zhou, L., Zhang, C., Zheng, X., Cao, J., Huang, Y., He, N., Zhou, G., Bai, Y., Xie, Z., Tang, Z., Wu, B., Fang, J., Liu, G., and Yu, G.: Effects of national ecological restoration projects on carbon sequestration in China from 2001 to 2010, P. Natl. Acad. Sci. USA, 115, 4039-4044, https://doi.org/10.1029/2018EF00089010.1073/pnas.1700294115, 2018.

Luo, T.: Patterns of net primary productivity for Chinese major forest types and their mathematical models, Chinese Academy of Sciences, 1996.

Luo, Y., Zhang, X., Wang, X., and Lu, F.: Biomass and its allocation of Chinese forest ecosystems, Ecology, 95, 2026-2026, https://doi.org/10.1890/13-2089.1, 2014.

506 Luo, Y., Wang, X., Zhang, X., Booth, T. H., and Lu, F.: Root:shoot ratios across China's forests: Forest type and
507 climatic effects, Forest Ecol. Manag., 269, 19-25, https://doi.org/10.1016/j.foreco.2012.01.005, 2012.

508 Ma, H., Mo, L., Crowther, T. W., Maynard, D. S., van den Hoogen, J., Stocker, B. D., Terrer, C., and Zohner, C.
509 M.: The global distribution and environmental drivers of aboveground versus belowground plant biomass, Nat.
510 Ecol. Evol., https://doi.org/10.1038/s41559-021-01485-1, 2021.

511 Mialon, A., Rodríguez-Fernández, N. J., Santoro, M., Saatchi, S., Mermoz, S., Bousquet, E., and Kerr, Y. H.:
512 Evaluation of the Sensitivity of SMOS L-VOD to Forest Above-Ground Biomass at Global Scale, Remote Sens.,
513 12, 1450, https://doi.org/10.3390/rs12091450, 2020.

514 Mokany, K., Raison, R. J., and Prokushkin, A. S.: Critical analysis of root: shoot ratios in terrestrial biomes, Global
515 Change Biol., 12, 84-96, https://doi.org/10.1111/j.1365-2486.2005.001043.x, 2006.

516 Niu, Q., Xiao, X., Zhang, Y., Qin, Y., Dang, X., Wang, J., Zou, Z., Doughty, R. B., Brandt, M., Tong, X., Horion,
517 S., Fensholt, R., Chen, C., Myneni, R. B., Xu, W., Di, G., and Zhou, X.: Ecological engineering projects increased
518 vegetation cover, production, and biomass in semiarid and subhumid Northern China, Land Degrad. Dev., 30,
519 1620-1631, https://doi.org/10.1002/ldr.3351, 2019.

520 O'Neill, P. E., Chan, S., Njoku, E. G., Jackson, T., Bindlish, R., and Chaubell, J.: SMAP Enhanced L3 Radiometer
521 Global Daily 9 km EASE-Grid Soil Moisture, Version 5., NASA National Snow and Ice Data Center Distributed
522 Active Archive Center. [dataset], https://doi.org/10.5067/4DQ54OUIJ9DL., 2021.

523 Qi, Y., Wei, W., Chen, C., and Chen, L.: Plant root-shoot biomass allocation over diverse biomes: A global synthesis,
524 Glob Ecol. Conserv., 18, e00606, https://doi.org/10.1016/j.gecco.2019.e00606, 2019.

525 Reich, P. B., Luo, Y., Bradford, J. B., Poorter, H., Perry, C. H., and Oleksyn, J.: Temperature drives global patterns
526 in forest biomass distribution in leaves, stems, and roots, P. Natl. Acad. Sci. USA, 111, 13721,
527 https://doi.org/10.1073/pnas.1216053111, 2014.

528 Saatchi, S. S., Harris, N. L., Brown, S., Lefsky, M., Mitchard, E. T. A., Salas, W., Zutta, B. R., Buermann, W.,
529 Lewis, S. L., Hagen, S., Petrova, S., White, L., Silman, M., and Morel, A.: Benchmark map of forest carbon stocks
530 in tropical regions across three continents, P. Natl. Acad. Sci. USA, 108, 9899,
531 https://doi.org/10.1073/pnas.1019576108, 2011.

532 Santoro, M., Cartus, O., Carvalhais, N., Rozendaal, D. M. A., Avitabile, V., Araza, A., de Bruin, S., Herold, M.,
533 Quegan, S., Rodríguez-Veiga, P., Balzter, H., Carreiras, J., Schepaschenko, D., Korets, M., Shimada, M., Itoh, T.,
534 Moreno Martínez, Á., Cavlovic, J., Cazzolla Gatti, R., da Conceição Bispo, P., Dewnath, N., Labrière, N., Liang,
535 J., Lindsell, J., Mitchard, E. T. A., Morel, A., Pacheco Pascagaza, A. M., Ryan, C. M., Slik, F., Vaglio Laurin, G.,
536 Verbeeck, H., Wijaya, A., and Willcock, S.: The global forest above-ground biomass pool for 2010 estimated from
537 high-resolution satellite observations, Earth Syst. Sci. Data, 13, 3927-3950, https://doi.org/10.5194/essd-13-3927-
538 2021, 2021.

539 Spawn, S. A., Sullivan, C. C., Lark, T. J., and Gibbs, H. K.: Harmonized global maps of above and belowground
540 biomass carbon density in the year 2010, Sci. Data, 7, 112, https://doi.org/10.1038/s41597-020-0444-4, 2020.

541 Su, Y., Guo, Q., Xue, B., Hu, T., Alvarez, O., Tao, S., and Fang, J.: Spatial distribution of forest aboveground

biomass in China: Estimation through combination of spaceborne lidar, optical imagery, and forest inventory data, Remote. Sens. Environ., 173, 187-199, https://doi.org/10.1016/j.rse.2015.12.002, 2016.

Tang, X., Zhao, X., Bai, Y., Tang, Z., Wang, W., Zhao, Y., Wan, H., Xie, Z., Shi, X., Wu, B., Wang, G., Yan, J., Ma, K., Du, S., Li, S., Han, S., Ma, Y., Hu, H., He, N., Yang, Y., Han, W., He, H., Yu, G., Fang, J., and Zhou, G.: Carbon pools in China's terrestrial ecosystems: New estimates based on an intensive field survey, P. Natl. Acad. Sci. USA, 115, 4021, https://doi.org/10.1073/pnas.1700291115, 2018.

Tong, X., Brandt, M., Yue, Y., Horion, S., Wang, K., Keersmaecker, W. D., Tian, F., Schurgers, G., Xiao, X., Luo, Y., Chen, C., Myneni, R., Shi, Z., Chen, H., and Fensholt, R.: Increased vegetation growth and carbon stock in China karst via ecological engineering, Nat. Sustain., 1, 44-50, https://doi.org/10.1038/s41893-017-0004-x, 2018.

Tong, X., Brandt, M., Yue, Y., Ciais, P., Rudbeck Jepsen, M., Penuelas, J., Wigneron, J.-P., Xiao, X., Song, X.-P., Horion, S., Rasmussen, K., Saatchi, S., Fan, L., Wang, K., Zhang, B., Chen, Z., Wang, Y., Li, X., and Fensholt, R.: Forest management in southern China generates short term extensive carbon sequestration, Nat. Commun., 11, 129, https://doi.org/10.1038/s41467-019-13798-8, 2020.

Wang, J., Feng, L., Palmer, P. I., Liu, Y., Fang, S., Bösch, H., O'Dell, C. W., Tang, X., Yang, D., Liu, L., and Xia, C.: Large Chinese land carbon sink estimated from atmospheric carbon dioxide data, Nature, 586, 720-723, https://doi.org/10.1038/s41586-020-2849-9, 2020.

Wang, L., Li, L., Chen, X., Tian, X., Wang, X., and Luo, G.: Biomass Allocation Patterns across China's Terrestrial Biomes, PLoS One, 9, e93566, https://doi.org/10.1371/journal.pone.0093566, 2014.

Wang, M., Fan, L., Frappart, F., Ciais, P., Sun, R., Liu, Y., Li, X., Liu, X., Moisy, C., and Wigneron, J.-P.: An alternative AMSR2 vegetation optical depth for monitoring vegetation at large scales, Remote. Sens. Environ., 263, 112556, https://doi.org/10.1016/j.rse.2021.112556, 2021a.

Wang, M., Wigneron, J.-P., Sun, R., Fan, L., Frappart, F., Tao, S., Chai, L., Li, X., Liu, X., Ma, H., Moisy, C., and Ciais, P.: A consistent record of vegetation optical depth retrieved from the AMSR-E and AMSR2 X-band observations, Int. J. Appl. Earth Obs., 105, 102609, https://doi.org/10.1016/j.jag.2021.102609, 2021b.

Wigneron, J.-P., Chanzy, A., Calvet, J.-C., and Bruguier, N.: A simple algorithm to retrieve soil moisture and vegetation biomass using passive microwave measurements over crop fields, Remote. Sens. Environ., 51, 331-341, https://doi.org/10.1016/0034-4257(94)00081-W, 1995.

Wu, X., Wang, S., Fu, B., Feng, X., and Chen, Y.: Socio-ecological changes on the Loess Plateau of China after Grain to Green Program, Sci. Total Environ., 678, 565-573, https://doi.org/10.1016/j.scitotenv.2019.05.022, 2019.

Xu, L., Saatchi, S. S., Yang, Y., Yu, Y., Pongratz, J., Bloom, A. A., Bowman, K., Worden, J., Liu, J., Yin, Y., Domke, G., McRoberts, R. E., Woodall, C., Nabuurs, G.-J., de-Miguel, S., Keller, M., Harris, N., Maxwell, S., and Schimel, D.: Changes in global terrestrial live biomass over the 21st century, Sci. Adv., 7, eabe9829, https://doi.org/10.1126/sciadv.abe9829, 2021.

Yang, D., Liu, Y., Feng, L., Wang, J., Yao, L., Cai, Z., Zhu, S., Lu, N., and Lyu, D.: The First Global Carbon Dioxide Flux Map Derived from TanSat Measurements, Ad. Atmos. Sci., 38, 1433-1443, https://doi.org/10.1007/s00376-021-1179-7, 2021.

Yang, J. and Huang, X.: The 30 m annual land cover dataset and its dynamics in China from 1990 to 2019, Earth Syst. Sci. Data, 13, 3907-3925, https://doi.org/10.5194/essd-13-3907-2021, 2021.

Yu, Z., Zhao, H., Liu, S., Zhou, G., Fang, J., Yu, G., Tang, X., Wang, W., Yan, J., Wang, G., Ma, K., Li, S., Du, S., Han, S., Ma, Y., Zhang, D., Liu, J., Liu, S., Chu, G., Zhang, Q., and Li, Y.: Mapping forest type and age in China's plantations, Sci. Total Environ., 744, 140790, https://doi.org/10.1016/j.scitotenv.2020.140790, 2020.

Zhang, R., Zhou, X., Ouyang, Z., Avitabile, V., Qi, J., Chen, J., and Giannico, V.: Estimating aboveground biomass in subtropical forests of China by integrating multisource remote sensing and ground data, Remote. Sens. Environ., 232, 111341, https://doi.org/10.1016/j.rse.2019.111341, 2019.

Zhang, Y., Yao, Y., Wang, X., Liu, Y., and Piao, S.: Mapping spatial distribution of forest age in China, Earth Space Sci., 4, 108-116, https://doi.org/10.1002/2016EA000177, 2017.